ELECTROCHEMISTRY

Single "Swiss-roll" microelectrode elucidates the critical role of iron substitution in conversion-type oxides

Lixiang Liu[1,2,3], Shaozhuan Huang[4]*, Wujun Shi[5], Xiaolei Sun[2,6], Jinbo Pang[7], Qiongqiong Lu[7], Ye Yang[8], Lixia Xi[7], Liang Deng[7], Steffen Oswald[7], Yin Yin[2], Lifeng Liu[9], Libo Ma[2], Oliver G. Schmidt[2,3,10], Yumeng Shi[1]*, Lin Zhang[11]*

Advancing the lithium-ion battery technology requires the understanding of electrochemical processes in electrode materials with high resolution, accuracy, and sensitivity. However, most techniques today are limited by their inability to separate the complex signals from slurry-coated composite electrodes. Here, we use a three-dimensional "Swiss-roll" microtubular electrode that is incorporated into a micrometer-sized lithium battery. This on-chip platform combines various in situ characterization techniques and precisely probes the intrinsic electrochemical properties of each active material due to the removal of unnecessary binders and additives. As an example, it helps elucidate the critical role of Fe substitution in a conversion-type NiO electrode by monitoring the evolution of Fe_2O_3 and solid electrolyte interphase layer. The markedly enhanced electrode performances are therefore explained. Our approach exposes a hitherto unexplored route to tracking the phase, morphology, and electrochemical evolution of electrodes in real time, allowing us to reveal information that is not accessible with bulk-level characterization techniques.

INTRODUCTION

To enhance the performance of lithium-ion batteries (LIBs), it is crucial to understand the electrochemical reaction mechanisms in the electrodes (1–3). For example, conversion-type electrodes (CTOs) have been considered a high-energy-density alternative to intercalation-type electrodes (4–6). However, they usually show complex reaction processes accompanied by the multireaction intermediates. This poses a substantial challenge to understanding their internal electrochemical reactions and ultimately improving the overall battery performance (7, 8). Hence, various in situ and in operando techniques have been developed during the past years, with the goal of characterizing the electrode materials during their operations (9, 10). Unfortunately, because of the use of slurry-coated composite electrodes (Fig. 1A), it is not possible to extract the electrochemical information directly for each individual active material in these experiments (fig. S1) (11, 12).

Microscale devices (13–15) are an emerging platform for studying the lithium storage mechanism in battery electrodes (16). They are capable of precisely probing the intrinsic electrochemical properties of each individual active material component because of the elimination of unnecessary binders and additives (17). Pioneering works include the in situ electron microscope investigations of the structural changes in nanostructured electrode materials (18, 19). However, microscale platforms have their own set of limitations, with the most important ones being (i) the extremely weak signal from the limited amount of materials under investigation and (ii) the often-observed spectral distortion due to background signals.

Here, we introduce a single "Swiss-roll" microelectrode platform. It can simultaneously perform in situ Raman spectroscopy, electrodynamic electrochemical impedance spectroscopy (EIS), optical microscopy, and electrochemical measurements during battery operations, yielding a comprehensive understanding of the energy storage processes. The electrode is prepared by rolling up a two-dimensional (2D) thin film into a 3D microtubular structure with multiwindings (20). The freestanding structure avoids laser excitation of the substrate and, hence, unwanted background signals and spectral distortion in Raman spectroscopy (21). The unique multiwinding structure produces a substantially enhanced Raman signal compared to a 2D thin film (22, 23). This type of microelectrodes will be a powerful tool to evaluate the active electrode materials with high resolution, accuracy, and sensitivity, allowing us to reveal information that is not accessible with bulk-level in situ characterization techniques.

To showcase the advantage of this platform, we have investigated a single iron-substituted NiO (NFO) microtubular electrode (Fig. 1). The critical role of iron substitution in the conversion-type NFO material is unveiled. It successfully explains the markedly enhanced performance of the NFO-based electrode when compared with an NiO-based control sample. We observed the growth of Fe_2O_3 and a thinner solid electrolyte interphase (SEI) layer during the initial lithiation/delithiation processes. In operando electrical measurements show that the lithium-ion diffusion coefficient in NFO is accelerated by fourfold compared to pure NiO at the fully

[1]International Collaborative Laboratory of 2D Materials for Optoelectronics Science and Technology of Ministry of Education Institute of Microscale Optoelectronics, Shenzhen University, Shenzhen 518060, China. [2]Institute for Integrative Nanosciences, IFW Dresden, Helmholtzstraße 20, 01069 Dresden, Germany. [3]Research Center for Materials, Architectures and Integration of Nanomembranes (MAIN), Technische Universität Chemnitz, Rosenbergstraße 6, 09126 Chemnitz, Germany. [4]Key Laboratory of Catalysis and Energy Materials Chemistry of Ministry of Education, South-Central Minzu University, 430074 Wuhan, China. [5]Center for Transformative Science, ShanghaiTech University, 201210 Shanghai, China. [6]School of Materials Science and Engineering, Nankai University, 300350 Tianjin, China. [7]Institute for Complex Materials, IFW Dresden, 01069 Dresden, Germany. [8]Center for Advancing Electronics Dresden and Faculty of Chemistry and Food Chemistry, Technische Universität Dresden, 01062 Dresden, Germany. [9]Clean Energy Cluster, International Iberian Nanotechnology Laboratory (INL), 4715-330 Braga, Portugal. [10]Nanophysics, Faculty of Physics, Technische Universität Dresden, 01062 Dresden, Germany. [11]Institut für Festkörperphysik, Leibniz Universität Hannover, D-30167 Hannover, Germany.
*Corresponding author. Email: yumeng.shi@szu.edu.cn (Y.S.); husz001@scuec.edu.cn (S.H.); l.zhang@fkp.uni-hannover.de (L.Z.).
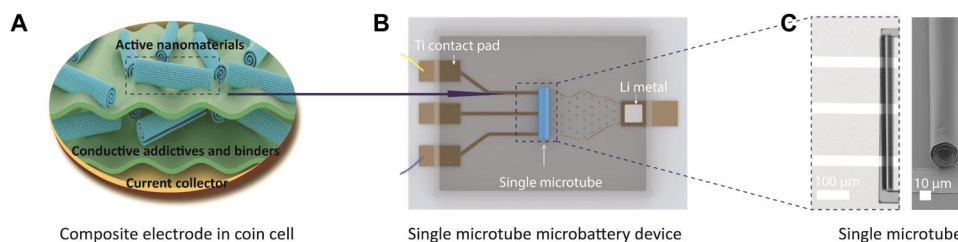
Fig. 1. Design of experiments. (**A**) Typical design of a composite electrode used in coin cells to confirm the superior rate capability and cyclability of NFO. It contains microtubular NFO nanomembranes, conductive additive, binder, and current collector. (**B**) An overview of a single microtube battery device. Three Ti contacts are integrated on one microtube battery to study the substitution mechanism on the conversion-type material during lithiation/delithiation. (**C**) Optical image of a single microtube battery device and (**D**) scanning electron microscopy (SEM) image of a single microtube with diameter of ~20 μm.

delithiated state. The lower electrical resistivity of NFO (approximately 1.5 times lower than that of pure NiO) corroborates the finding of a thinner SEI layer in the Raman measurements. These results are responsible for the faster charge-transfer reaction rates, thereby explaining an excellent rate performance of NFO: 440 mA·hour g^{-1} at a high rate of 20 A g^{-1}.

RESULTS AND DISCUSSION
Extraordinary performances of NFO microtube electrodes
To evaluate the lithium storage performance of NFO, we first prepared the composite electrodes by mixing the microtubes with conductive additives and binders in a typical coin cell configuration (see Fig. 1A and Materials and Methods). The morphology and elemental composition of multiple rolled-up microtubes are investigated by scanning electron microscopy (SEM; Fig. 2A) and energy-dispersive x-ray (EDX) analysis (fig. S2, A and B). The rate capacities of NFO are compared with NiO and Fe_2O_3 microtubes at different current densities. As shown in Fig. 2B, the NFO delivers much better rate capability than the NiO and Fe_2O_3 microtubes. Specifically, at a high current density of 20 A g^{-1}, NFO delivers a high specific capacity of 452 mA·hour g^{-1}, which is more than four times that of NiO (111 mA·hour g^{-1}), indicating that Fe substitution can greatly promote the Li^+ transfer kinetics. When the current density drops to 0.2 A g^{-1}, the reversible capacity returns to 819 mA·hour g^{-1} for NFO but only 357 mA·hour g^{-1} for NiO. The corresponding galvanostatic charge-discharge profiles of NiO and NFO electrodes at various current densities are shown in fig. S3. After the rate capability test, the NFO electrode was cycled at 1 A g^{-1} for more than 1600 cycles (Fig. 2C), and no capacity fading was observed. In contrast, both NiO and Fe_2O_3 electrodes exhibit a rapid capacity fading. Furthermore, the electrochemical performances of NFO with varying concentrations of Fe substitution are investigated in fig. S4. The results suggest that the NFO with 30 atomic % (at %) of Fe is the most optimized substitution.

To our knowledge, this is among the most stable performance for the conversion-type LIB electrodes. These results demonstrate that the lithium storage performance of NFO is largely improved by the Fe substitution, but the more difficult question is what are the mechanisms behind it? The answer to this question may shed new light on developing advanced CTO materials. The composite electrodes, however, are unsuitable for this type of investigation. Therefore, we propose an in situ/in operando platform based on a single microtube to elucidate the critical role of iron substitution (see Fig. 1B).

Structural, compositional analyses and enhanced Raman scattering
A single microtube–based LIB device was fabricated using the processes shown in Fig. 2D (see the Supplementary Materials for details). It is essential to control the rolling direction of the nanomembrane to integrate the rolled-up microtube into an on-chip device. For this purpose, we performed three steps of lithography. First, a blank square of 340 μm by 480 μm was patterned on a glass substrate, followed by the deposition of a 20-nm Ge sacrificial layer (Fig. 2D, a). Second, a photoresist layer was patterned to seal three edges of the Ge layer, which leaves one open edge for the rolling process. Then, the Ni-Fe bimetallic oxide layer was deposited onto the Ge sacrificial layer by evaporating ferronickel (Ni_7Fe_3) under an O_2 atmosphere (Fig. 2D, b). Last, 50-nm-thick Ti electrical contacts were deposited and served as the current collectors. After that, the whole sample was immersed in deionized water to slowly dissolve the Ge sacrificial layer (Fig. 2D, c). The EDX spectrum confirms the complete dissolution of the Ge sacrificial layer (fig. S5) after etching. During this process, the built-in strain was released, and the NFO nanomembrane rolled up into a microtubular structure with multiwindings (Fig. 2D, d and e) (24, 25).

Figure 2E is the SEM image of a single NFO microtube with a length of 480 μm and a diameter of 20 μm. The cross-sectional SEM image reveals a Swiss-roll structure with multiple windings (Fig. 2F). The EDX elemental maps show that the Ni, Fe, and O elements are uniformly distributed (Fig. 2G). According to the transmission electron microscopy (TEM) image (Fig. 2H), the NFO nanomembrane consists of many nanoparticles and voids, proving the polycrystalline nature of the nanomembranes. The x-ray diffraction (XRD) pattern (fig. S6A) reveals that the main composition of NFO is cubic NiO [Joint Committee on Powder Diffraction Standards (JCPDS) no. 47-1049]. The NFO shows the same selected-area electron diffraction pattern (Fig. 2I) as NiO (fig. S7), corresponding to the (001), (200), and (111) planes of polycrystalline cubic phase of NiO, respectively. Furthermore, the high-resolution TEM image reveals well-resolved lattice fringes with an interplanar spacing of 0.211 nm, belonging to (200) planes of cubic structure NiO (Fig. 2J). However, compared with the pure NiO sample, the NFO sample has lower 2θ angles for the XRD diffraction peaks (fig. S6B), which can be explained by the lattice expansion due to the Fe substitution.

By using x-ray photoelectron spectroscopy (XPS), the high-resolution Ni 2p spectrum shows a pair of doublet peaks at 855.2 and 872.8 eV, corresponding to the Ni $2p_{3/2}$ and Ni $2p_{1/2}$ states (26). The peaks at 861.2 and 879.6 eV are the satellite peaks of the Ni^{2+} state
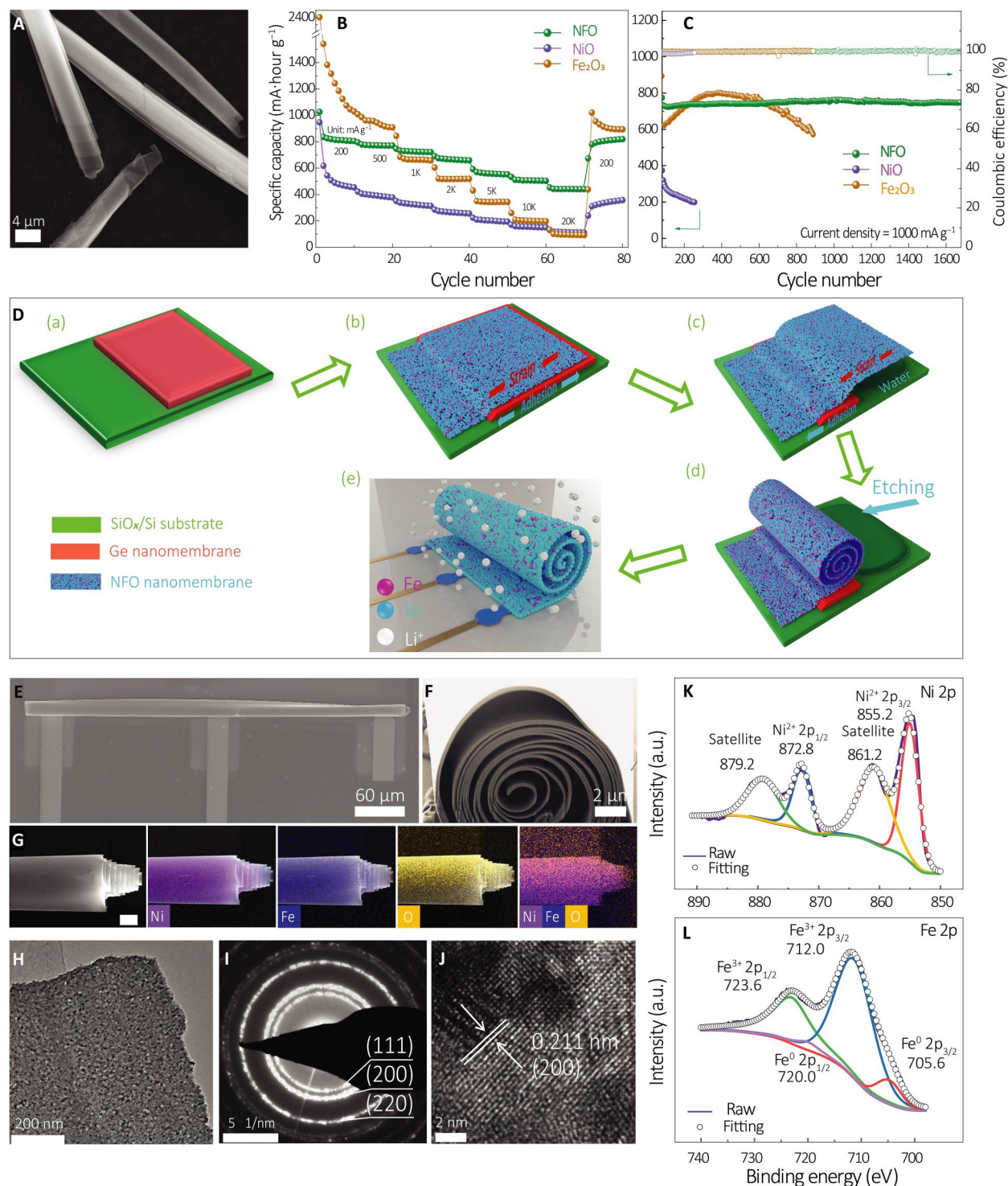
Fig. 2. Large-scale preparation of single microtubes for electrochemical performance analysis in the coin cell and morphological and phase characterization of single microtubes. (**A**) SEM image of rolled-up NFO microtubes. Electrochemical tests were first performed with the composite electrodes in the coin cell configuration. (**B**) Rate capability of NFO, NiO, and Fe_2O_3 composite electrodes at different current densities. (**C**) Long-term cycling stability of NFO, NiO, and Fe_2O_3 composite electrodes at a current density of 1000 mA g^{-1}. (**D**) Schematic illustration of the fabrication flow of a single NFO rolled-up microtube. (**E**) SEM top view of a single NFO rolled-up microtube. (**F**) Cross-sectional view of a single rolled-up microtube. (**G**) Elemental mapping of Ni (purple), Fe (blue), and O (yellow). Scale bar, 5 μm. (**H**) TEM image, (**I**) the corresponding selected-area electron diffraction pattern, and (**J**) high-resolution TEM image of NFO. (**K**) Ni 2p and (**L**) Fe 2p x-ray photoelectron spectroscopy (XPS) spectra of NFO. The carbon C 1s peak at 284.8 eV was used as a reference to correct the peak shifts. a.u., arbitrary units.

(Fig. 2K). The XPS spectrum of Fe 2p is shown in Fig. 2L, where the peaks with higher binding energy (712.0 and 723.6 eV) are assigned to the Fe^{3+} $2p_{3/2}$ and Fe^{3+} $2p_{1/2}$ states, while the doublet at 705.6 and 720.0 eV is from a residual of elemental Fe, corresponding to the Fe^0 $2p_{3/2}$ and Fe^0 $2p_{1/2}$ states. The area ratio between Fe^0 2p3/2 and Fe^{3+} 2p3/2 is approximately 7:100, indicating that Fe^{3+} substitution is the predominant composition of element Fe in NFO. Inductively coupled plasma (ICP) elemental analysis reveals that the accurate Ni/Fe element ratio is around 7.2:2.8, being close to the ratio of the original Ni_7Fe_3 target. Thus, the chemical formula of NFO can be written as $Ni_{0.72}Fe_{0.28-\delta}O$. Raman spectra also confirm the successful incorporation of Fe ions in the NiO crystal (fig. S8). The one-phonon (1P) band (27) shifts from 515 cm^{-1} for NiO to a higher wave number of 577 cm^{-1} for NFO. This result is consistent with a previous report (28). The 2P band (27) on the other hand shifts from 650 cm^{-1} for NiO to 690 cm^{-1} for NFO.

After the structural and compositional analyses, we evaluate the enhanced Raman scattering in the NFO microtube. Figure 3A shows two different regions for the measurements. The red rectangle marks the flat NFO thin film, while the green rectangle marks the rolled-up NFO microtube. Figure 3 (B and C) shows the Raman spectra contour maps for these two regions, displaying very clear differences. For the thin-film region, the Raman signal from NFO was too weak to be detected, and only a strong peak at 520 cm^{-1} from the Si/SiO$_x$ substrate can be observed (Fig. 3B). For the

microtube region, the Raman signal from NFO is very intense and overwhelms the substrate signal (Fig. 3C).

This notably enhanced Raman scattering allows detailed investigations of LIB electrodes based on the single Swiss-roll microtube electrodes. Therefore, we fabricated micrometer-sized Li battery (MLB) devices with these electrodes. A Li foil was used as the reference electrode. Figure 3D shows a schematic setup of the MLB platform (see Materials and Methods and fig. S9). The optical images are shown in Fig. 3E.

In situ Raman spectroscopy unveils the role of Fe substitution

To investigate the electrochemical mechanisms in NFO, in situ Raman spectroscopy was performed during the lithiation/delithiation processes within the voltage window of 0.01 to 3 V (versus Li$^+$/Li). Figure 4 (A and B) shows the simultaneous evolution of the Raman spectra and the corresponding cyclic voltammetry (CV) curves during the first lithiation/delithiation cycle (fig. S10 shows the CV curve in a full cycle). To obtain a better overview of the chemical reactions, the Raman spectra are also shown as contour plots in Fig. 4C. At the early stage of lithiation (discharge from 3.0 to 1.0 V), a reversible phase change occurs, as $Ni_{0.72}Fe_{0.28-\delta}O$ changes to $Li_xNi_{0.72}Fe_{0.28-\delta}O$ upon the Li insertion (29). During this process, the two peaks corresponding to the Ni-O bonds [the 1P and 2P modes in Fig. 4 (A and C)] do not experience substantial changes. Similar behaviors can be also observed for the
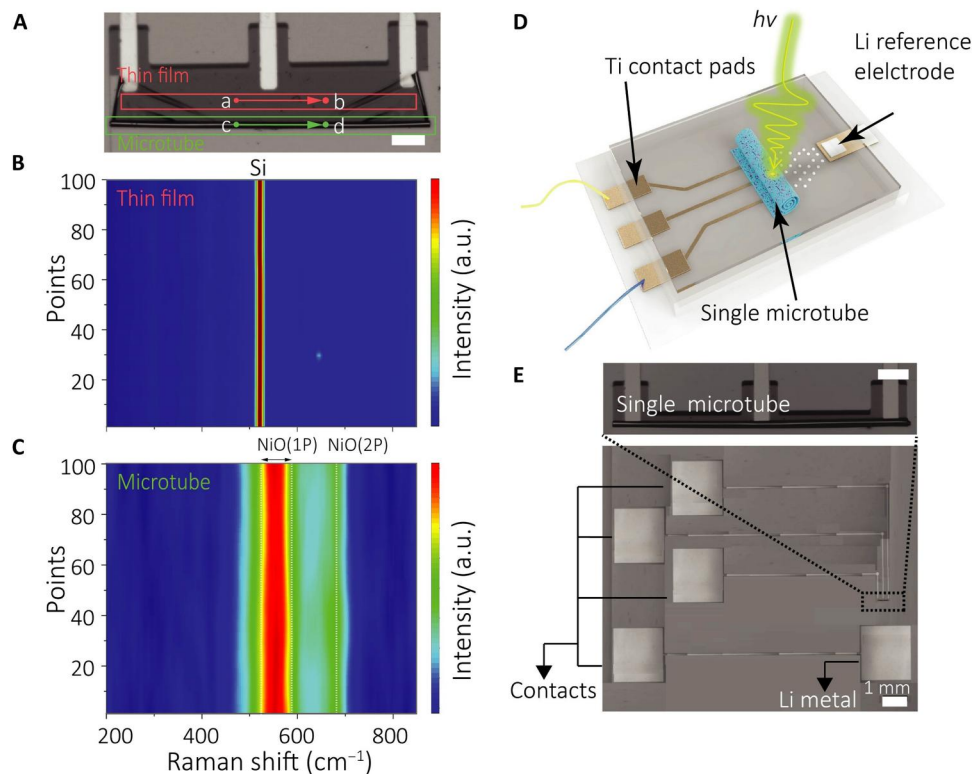

Fig. 3. Single microtube devices for in situ measurements. (**A**) Optical image of an NFO microtube as marked with a green rectangle. The thin film area is marked in the red rectangle. Raman spectra at different positions of (**B**) NFO thin film and (**C**) NFO rolled-up nanomembrane. Raman spectra are collected along with the red and green arrows from point a to point b and from point c to point b, as indicated in (A). (**D**) Schematic illustration of the microbattery device based on a single NFO microtube electrode. (**E**) Optical image of a microbattery with multiple large contacts and the Li reference electrode. The inset image shows a microtube attached to three contacts. Scale bars, 50 μm (A and E).
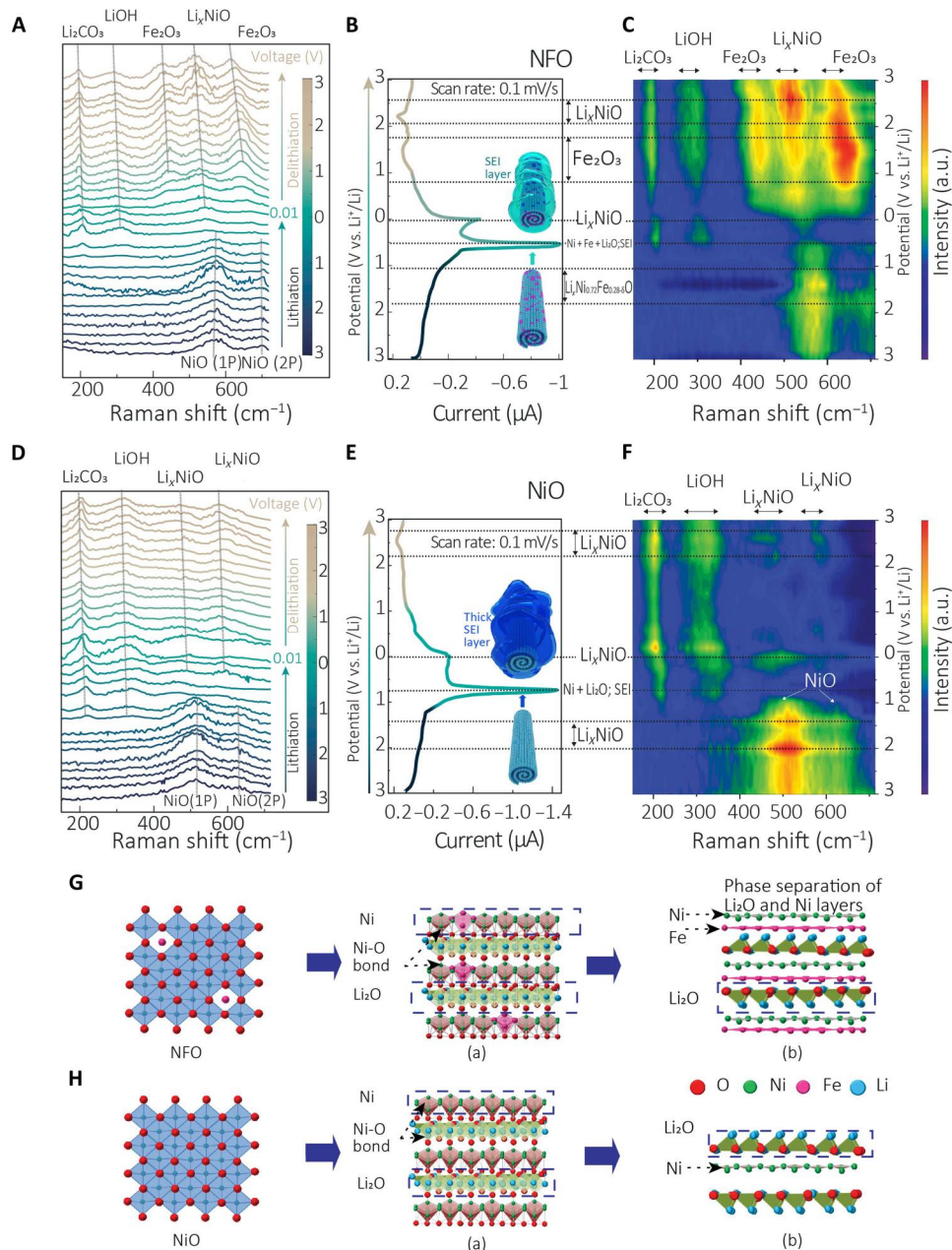
Fig. 4. In situ Raman spectroscopic evolution based on the single microtube devices. In situ Raman spectroscopic evolution of (**A**) single NFO microtube and (**D**) single NiO microtube with the applied potential varied from 3 V (versus Li$^+$/Li) to 0.01 V (versus Li$^+$/Li) and then back to 3 V (versus Li$^+$/Li). The dashed lines indicate the evolution of the major Raman modes. The potentials of each spectrum are indicated by the color bar. Corresponding CV curves were acquired during the Raman measurements and are shown in (**B**) and (**E**). Insets are the schematics of morphology evolution on the formation of SEI layer for NFO and NiO during lithiation. For a better overview, the Raman spectra are also shown in the contour plots in (**C**) and (**F**). Schematic diagrams of the structure and phase evolution of NFO and NiO during lithiation are shown in (**G**) and (**H**), respectively.

unsubstituted NiO within the voltage window of 3.0 to 1.5 V (versus Li$^+$/Li; Fig. 4F and eq. S1). At around 0.5 V, the NiO signal disappears for the NFO microtube, accompanied by the appearance of an SEI layer signal. The phase changes imply the full reduction of Ni ions to metallic Ni^0. Together with the breakage of Ni-O bonds, the phase separation occurs between Ni^0 and Li$_2$O [see process (b) in Fig. 4G; Eq. 3] (29). Here, the Fe substitution acts as a barrier to

prevent Ni coarsening. Therefore, abundant Ni/Li$_2$O interfaces can exist in the lithiated materials (Fig. 5H).

In the delithiation process, we observe two new Raman modes at 443 cm^{-1} (T$_{2g}$) and 644 cm^{-1} (A$_{1g}$) as the voltage approaches 0.6 V (versus Li$^+$/Li; Fig. 4C). These are the characteristic peaks of the Fe$_2$O$_3$ spinel structure (30), which is evidence for the oxidation of Fe^0 to Fe^{3+} during the lithiation process. The reaction can be
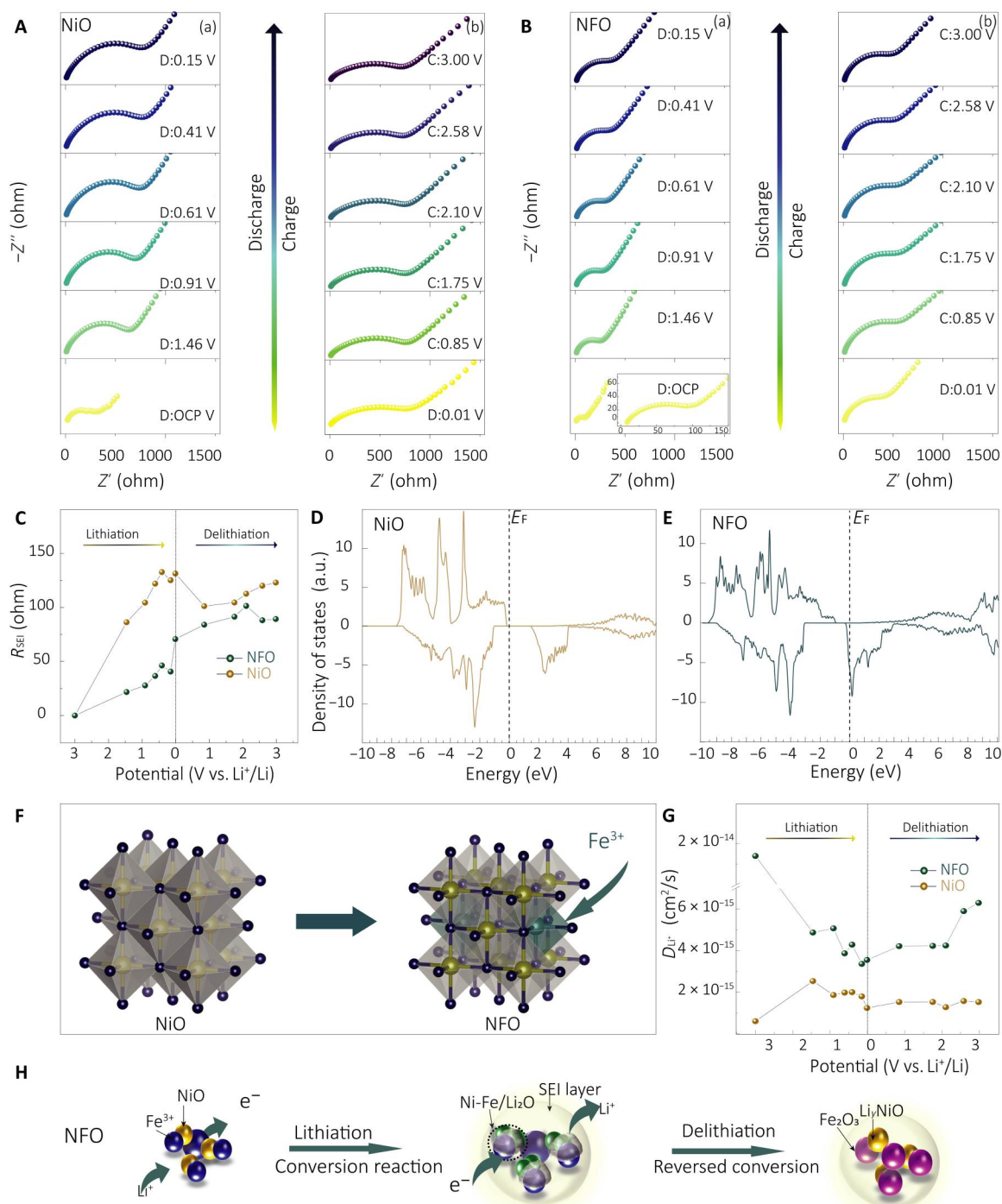
Fig. 5. In situ EIS measurements based on the single microtube devices and DOS calculations and analysis. In situ EIS of NiO (**A**) and NFO (**B**) during the initial cycle (a, the lithiation process; b, the delithiation process; OCP, open circuit potential). (**C**) R_{SEI} as a function of the potential voltage during the first lithiation and delithiation processes. (**D** and **E**) Calculated partial electronic densities of states (DOS) for NiO and NFO. The zero energy level in DOS diagrams represents the position of Fermi energy and is shown by a vertical dashed line. (**F**) Optimized structures for NiO and NFO from VESTA software (*56*). Yellow atoms represent Ni^{2+}; blue atoms represent O^{2-}, and green atoms represent Fe^{3+}. (**G**) Lithium-ion diffusion coefficients under different potential voltages. (**H**) Schematic showing the structure and phase evolution of NFO electrode during initial discharge and charge, featuring the formation of Ni/Fe and Li_2O during discharge.
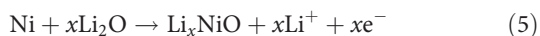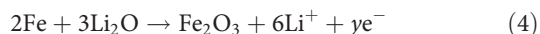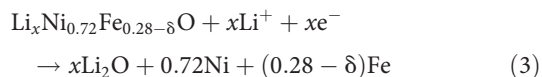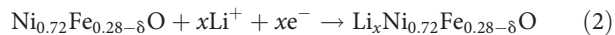
described by Eq. 1

$$2Fe + 3Li_2O \rightarrow Fe_2O_3 + 6Li^+ + 6e^- \qquad (1)$$
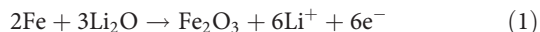
TEM characterization (fig. S11) also proves the formation of the Fe_2O_3 phase (31). The characteristic peaks of Fe_2O_3 increase gradually with further delithiation, accompanied by a broad anodic peak at ~2.2 V (versus Li^+/Li) in Fig. 4B. During the first delithiation, the phase change of the iron substitution enhances the reversible decomposition of Li_2O, thus contributing to an extra Li storage capacity for NFO (32, 33).

We observed a notable blue shift for the Raman peaks associated with Fe_2O_3 and Li_xNiO during the delithiation. When the potential increases from 0.6 to 3.0 V (versus Li^+/Li), the T_{2g} and A_{1g} bands of Fe_2O_3 (at ~443 and 644 cm^{-1}) blue shift to 422 and 611 cm^{-1}, respectively. The peak at 545 cm^{-1}, which is associated with Li_xNiO, shifts to 512 cm^{-1} as the potential increases from 0.4 to 3.0 V (versus Li^+/Li). These blue shifts strongly suggest that the lengths of the reconstructed Ni-O and Fe-O bonds are changed during the delithiation process (34, 35). Moreover, the optical image shows that the whole NFO microtube stays intact after delithiation and exhibits a slightly wrinkled structure (because of the release of stress) at the fully delithiated state [inset of fig. S12A (d)] (12) and will be recovered to a loose tubular structure [fig. S12A (e)] at the fully lithiated state in the second cycle. These results prove that the rolled-up nanomembrane can well accommodate the volume change during lithiation/delithiation.

On the other hand, for the unsubstituted NiO microtube, the oxidation of metallic Ni appears at ~2.2 V (versus Li^+/Li; Fig. 4E), and the Ni-O bond Raman peaks (at 466 and 552 cm^{-1}; see Fig. 4F) gradually disappear at ~2.4 V (versus Li^+/Li). On the basis of the Raman spectra analysis, the complete electrochemical reactions of NFO can be summarized below

$$Ni_{0.72}Fe_{0.28-\delta}O + xLi^+ + xe^- \rightarrow Li_xNi_{0.72}Fe_{0.28-\delta}O \qquad (2)$$

$$Li_xNi_{0.72}Fe_{0.28-\delta}O + xLi^+ + xe^- \\ \rightarrow xLi_2O + 0.72Ni + (0.28-\delta)Fe \qquad (3)$$

$$2Fe + 3Li_2O \rightarrow Fe_2O_3 + 6Li^+ + ye^- \qquad (4)$$

$$Ni + xLi_2O \rightarrow Li_xNiO + xLi^+ + xe^- \qquad (5)$$

During the lithiation process, a very strong cathodic peak appears at around 0.5 V (versus Li^+/Li) and indicates the formation of the SEI layer (36). Correspondingly, two new Raman peaks, which are associated with LiOH and Li_2CO_3 (37), appear at 197 and 230 cm^{-1}, respectively. This result implies that LiOH and Li_2CO_3 are the main inorganic components in the SEI layer on NFO. Because of the partial decomposition of the electrolyte-permeable organics (38), the intensities for these SEI-related peaks decrease gradually with the lithiation process (Fig. 4A). In comparison, the Raman modes of the SEI layer are also detected for NiO at ~0.8 V (versus Li^+/Li). Note that the Raman peaks of the SEI layer in the NiO microtube always exist in the anodic scan (Fig. 4F). During the delithiation process, their intensities are much higher than those of the NFO, indicating the formation of a thicker

SEI layer (39). By contrast, the new phases upon the delithiation of NFO, i.e., Fe_2O_3 and Li_xNiO, show higher intensities because of the negligible background signal from the SEI layer. These results indicate that the formation of a thinner SEI layer and Fe_2O_3 could account for the enhanced initial Coulombic efficiency and the higher specific capacity of NFO. To reveal the SEI evolution, we performed the TEM at different stages (fig. S13). After recharging to 3.0 V, a uniform SEI layer of 11 nm adheres to the NFO electrode surface (fig. S13B). The thickness of the SEI layer still remains at 10 nm after 10 cycles, demonstrating the robust SEI layer on the NFO electrode (fig. S13D). In contrast, the NiO electrode shows a thicker SEI layer of 29 nm after the initial cycle (fig. S13A) and a nonuniform SEI layer after 10 cycles (fig. S13C). The SEI evolution of NFO and NiO verifies that the SEI film on the NFO surface is thinner and more stable than on NiO surface.

EIS measurement and density-of-states calculation of interfacial kinetics

To further elucidate the kinetic effect of the Fe substitution in the single NFO microtube, we performed in situ EIS. The cell was allowed to rest for 20 min before recording each spectrum. Figure 5 (A and B) plots the EIS spectra during the discharging/charging processes of NFO (the imaginary components are shown in fig. S14). The EIS data are fitted with an equivalent circuit that includes a resistor of the electrolyte (R_s), a resistor of the SEI layer (R_{SEI}), a charge transfer resistor (R_{ct}), a constant phase element, and a Warburg resistor (Z_W; fig. S15). The simulated results of NFO and NiO are listed in table S2. The variations of the R_{SEI} and R_{ct} at different polarization potentials are shown in Fig. 5C and fig. S16, respectively.

Over the entire lithiation/delithiation process, NFO shows a lower R_{ct} than NiO (fig. S16), suggesting that the Fe^{3+} substitution facilitates the charge transfer at the electrode/electrolyte interface. It forms a homogenous conductive network in the electrode and promotes electron transfer kinetics (40). As the lithiation proceeds, R_{ct} of both NFO and NiO increase obviously (by approximately threefold and approximately sixfold for NFO and NiO at ~0.01 V, respectively) because of the formation of the insulating SEI layer and Li_2O. During the delithiation process (from 0.01 to 0.85 V), R_{ct} of NFO shows an increase from 313.20 to 453.30 ohms due to the formation of Fe_2O_3 (as observed in the in situ Raman spectroscopy).

Unlike R_{ct}, R_{SEI} shows different trends for NiO and NFO (Fig. 5C). During delithiation process, it increases monotonically from 70.60 ohms (~0.01 V) to 101.50 ohms (~2.10 V) for NFO. Above 2.1 V, the delithiation process is attributed to the formation of NiO from Ni and Li_2O in NFO. The R_{SEI} of NFO is reduced as a result of this process. The possible reason is the partial decomposition of the outer layer (organic layer) and formation of lithium-ion conductive Li_2CO_3 of the SEI layer, which is confirmed with TEM observations (fig. S17). By contrast, R_{SEI} of NiO first decreases to 101.30 ohms (~0.85 V) and then increases to 123.10 ohms (~3.0 V). This abnormal behavior is corroborated by the observation of a thicker SEI layer on NiO in the Raman experiments in Fig. 4 (C and F). The thicker SEI layer (and, hence, the larger R_{SEI}) tends to break during the volume expansion process, which, in turn, exposes the fresh electrode material and leads to further growth of the SEI layer (41).

Density-of-states (DOS) calculations were then performed to further investigate the influence of iron substitution. Twenty-five

percent of Fe concentration (it is close to the experimental substituting content of 28%) is applied for the calculation to estimate the influence of Fe substitution. NiO shows a typical semiconducting character with a bandgap of 1.50 eV for spin-up and spin-down channels (Fig. 5D). After incorporating Fe^{3+} into NiO, we calculate the conventional cell of NiO with 1/4 Ni substituted by Fe (see Fig. 5F) and induce a lattice expansion in NiO. It shows a considerable rearrangement of states of NiO as shown in the DOS of NFO (Fig. 5E), creating a high DOS at the Fermi level owing to the highly localized d orbitals (42). The higher Fermi energy indicates an improved electrical conductivity and electrodynamics of NFO. In addition, the results indicate that Fe^{3+} is an acceptor substitution, with an unoccupied state above the Fermi surface (43), causing a large spin-split of the acceptor band, which can store lots of electrons based on Maier's theoretical model of space charge storage (44, 45), in favor of the Li^+ diffusion and storage during lithiation (46).

The lithium storage performance is closely related to the Li^+ diffusion processes. The designed microdevice allows a better understanding of the Li^+ diffusion behavior in single NFO and NiO microtubes by separating the bulk and interfacial Li^+ transport processes. In our work, the trends of D_{Li+} (lithium-ion diffusion coefficient) are consistent with previous literature reports (47–49). D_{Li+} in the NFO microtube approaches 6.29×10^{-15} cm^2 s^{-1} (~3.0 V) at the end of the charging process (Fig. 5G), which is four times higher than that in the NiO microtube (1.52×10^{-15} cm^2 s^{-1}; ~3.0 V; see the specific calculation of D_{Li+} in fig. S18). It indicates faster kinetics during charge storage of NFO, consequently accelerating the electrode reactions and enhancing the rate capability (50). The lower internal resistance and faster Li^+-ion diffusion of NFO support our hypothesis that the Fe conductive network provides an electron pathway, promoting its reversion into Li_xNiO in the Li_2O/Ni mixture. As shown in Fig. 5H, the $Li_xNi_{0.68}Fe_{0.28-\delta}O$ is converted to an Ni/Fe-Li_2O matrix with a thinner SEI layer, consequently preventing the aggregation of the active phases (Ni and Li_2O), maintaining fast reaction kinetics at the high-density Ni/Li_2O interfaces (31) and promoting the full conversion reactions of NiO.

Last, we evaluate the Li storage performance of NFO in a Li battery based on a single NFO microtube. Figure S19 shows the cyclability of the NFO and NiO microtube electrodes at a current density of 150 μA cm^{-2}. The specific reversible capacity of NFO after 30 cycles is 524 μA·hour cm^{-2}, much higher than that of NiO (78 μA·hour cm^{-2}). The reversible capacity of the NFO microtube remains almost constant, with a Coulombic efficiency of over 98% from the fifth cycle. The battery performance of the NFO microtube demonstrates a substantial enhancement of the Li storage capacity and cycling stability compared to that of NiO.

In addition, the versatility of the Swiss-roll microelectrode has also been demonstrated in the alloy-type and intercalation-type anode materials. As shown in fig. S20, typical single Si microtube (alloy-type) and single TiO_2 microtube (intercalation-type) are prepared with the same procedure as NFO. CV curves and real-time morphologic evolution of the single Si/TiO_2 microtubes at different potentials have been conducted (see details in the Supplementary Materials). We expect that the in situ techniques reported here can be readily applied to studying a range of other electrode materials, the outcomes of which will provide substantial insights into the corresponding battery technologies.

Single Swiss-roll microtubes are proposed as an ideal in situ/in operando platform to study the electrical conductivity, electrochemical reactions, and morphology evolution in battery electrodes. To showcase its advantages, we have investigated a single NFO microtubular electrode. The in situ Raman spectroscopy with enhanced signals revealed an unparalleled level of detail. In conjunction with electrochemical tests, they help capture the evolution processes of the Fe_2O_3 and SEI layers during the battery operation and thus explain the markedly enhanced redox kinetics and cycling stability in NFO. The results are further corroborated by in situ EIS studies and DOS calculations. These findings unveil the critical role of iron substitution and help us understand the mechanisms of capacity fading and reaction kinetics in CTOs. Therefore, the proposed platform facilitates the study of electrode evolution in otherwise inaccessible device configurations and, because of its miniaturized size, may also find applications in building self-powered microelectronic devices.

MATERIALS AND METHODS
Preparation of single NFO and NiO microtubes
Briefly, three steps of lithography were carried out. In the first lithography step, we patterned a blank square on a Si/SiO_x substrate, and then, a 20-nm Ge layer was deposited by using Ge as the target onto the square by electron beam evaporation (fig. S21A) as a sacrificial layer. The deposition speed was controlled at 1 Å s^{-1} under a pressure of 6×10^{-6} mbar. To realize directional roll-up of nanomembranes, the second lithography was performed to define a patterned photoresist and seal three edges of the Ge layer and the area around it. This will offer one open window during the tube rolling process. The sample was treated in oxygen plasma (10 min/50 W) and then baked overnight on a hotplate at 60°C to oxidize the Ge layer into GeO_x for facile etching in water. To ensure the cleanliness of the GeO_x layer and Si/SiO_x substrate, the aforementioned procedures are performed in the clean room. After that, an NFO or NiO layer was deposited using the alloy Ni_7Fe_3 or Ni as the target (fig. S21B) by electron beam evaporation (BOC Edwards FL400). The deposition speed was controlled at 0.5 Å s^{-1} with O_2 atmosphere under a pressure of 1.2×10^{-4} mbar. The final lithography step involves the patterning of the contact pads. Ti (50 nm) was subsequently deposited using Ti as the target by sputtering (nanoPVD) at a pressure of 4×10^{-5} mbar (fig. S21C). The sample was immersed in deionized H_2O for 2 hours for the directional rolling (fig. S21D) (51). The NFO and NiO nanomembrane self–rolled up from the long edge with the opened window (fig. S21B).

Assembly of the MLB platform with a single NFO rolled-up microtube as the anode
A single NFO microtube and a lithium layer were used as the anode and counter electrode, respectively. Polydimethylsiloxane (PDMS) was used for cell sealing. A PDMS mixture solution (1:10; SYLGARD 184 Silicone Elastomer Kit; Dow Corning, MI, USA) with a height of 1 mm and diameter of 5 mm was fixed around the NFO electrode. Afterward, the PDMS mold was treated by oxygen plasma for 30 s at 50 W, ensuring that the PDMS can be fixed firmly on the top of the Si/SiO_x substrate. Then, the device was transferred into an Ar-filled glove box [H_2O < 0.1 parts per million (ppm); O_2 < 0.1 ppm; MBRAUN, Germany]. A drop of melting Li metal was transferred on the top of the Ti contact pad. Once the lithium metal was cooled down, a small amount of electrolyte consisting of 1 M $LiPF_6$, ethylene carbonate, and dimethyl

carbonate (1:1 by weight) was then filled into the device chamber of the PDMS mold. A cleaning quartz plate with a thickness of 1 mm was used to cover the top of PDMS mold.

Bulk preparations of NFO and NiO microtubes

Positive photoresist (AR P3510; Allresist GmbH) as a sacrificial layer was spin-coated on a Si wafer at 4500 rpm for 50 s, followed by baking at 90°C for 5 min. The NFO and NiO nanomembranes (30 nm) were then deposited by electron beam evaporation (PVD 75; Kurt J. Lesker Company) at a current of 10 mA (10 kV) using alloy Ni_7Fe_3 and Ni as the target, respectively. The deposition speed was controlled to 0.5 Å s^{-1} with an O_2 atmosphere under pressure at 1.5×10^{-4} mbar. The resulting NFO and NiO microtubes were subsequently self–rolled up in acetone, respectively. As-synthesized rolled-up microtubes were collected and dried in a critical point dryer [(CPD); Autosamdri-931; Tousimis Research Corporation)].

Material characterization

XRD [Co Kα radiation (λ = 1.7890 Å); X'Pert PRO MPD, Philips] was used to analyze the crystal structures. Raman spectra were collected using a Raman microscope with a laser wavelength of 600 nm (LabRAM HR Evolution, HORIBA Scientific). The microstructure and morphology were characterized by field-emission SEM (DSM 982 Gemini, Germany) and TEM (FEI Titan ChemiSTEM 80-200). XPS was done using monochromatized Al-Kα radiation and a hemispherical analyzer at a pass energy of 29 eV (PHI 5600 CI, Physical Electronics, USA).

In situ Raman and electrochemical characterizations

For in situ Raman spectroscopy measurements, Li foil and single NFO nanomembranes were applied as the counter electrode and the working electrode, respectively. CV measurements during in situ Raman spectroscopic acquisitions were performed at room temperature using an electrochemical workstation (Multi Autolab/M101, Germany). Raman spectra were collected using a Raman microscope with a laser wavelength of 600 nm (LabRAM HR Evolution, HORIBA Scientific) with a 20× objective.

Coin cell material preparation and assembly

The electrochemical characterization of bulk NFO microtube samples were performed using coin-type cells. Li foil was used as the counter/reference electrode. The electrolyte was 1 M LiPF$_6$ dissolved in a mixture of ethylene carbonate and dimethyl carbonate (1:1 by weight; Merck). Celgard 2400 polypropylene was used as the separator. The conventional NFO nanomembrane electrode was prepared by mixing the active material, carbon black, and polyvinylidene fluoride at a weight ratio of 7:2:1 in distilled water. The resultant slurry was pasted onto a copper foil and dried in a vacuum oven at 100°C for 12 hours. All cells were assembled in an argon-filled glove box (H_2O < 0.1 ppm; O_2 < 0.1 ppm; MBRAUN, Germany). The charge/discharge profiles were tested by an Arbin BT2000 system. All other electrochemical measurements were performed in the electrochemical workstation (Multi Autolab/M101, Germany). The active mass loadings of NiO and NFO are 1.52 and 1.58 mg cm^{-2}, respectively, for the rate studies.

In situ EIS

EIS was adopted to record the change in the impedance spectra at different electrochemical states in the first cycle. The CV measurements were set to ensure that the reactions achieved equilibrium. The cell was allowed to rest for 60 min before collecting the EIS spectra.

Density functional theory calculations

Density functional theory based calculations were conducted with the Vienna Ab initio Simulation (VASP) package (52). VASP is a periodic plane wave code, in which the electron-ion interaction is described by the projector augmented wave method (53, 54). The exchange and correlation were accounted for by the generalized gradient approximation in the formulation of Perdew, Burke, and Ernzerhof (55). The kinetic energy cutoff was set as 600 eV. The Γ-centered $20 \times 20 \times 20$ k-points were used in the first Brillouin sampling. In NFO, we calculate the conventional cell of NiO with 1/4 Ni substituted by Fe. The structure was relaxed using a force less than 0.1 eV/Å. Spin polarization was considered in all calculations.

Supplementary Materials

This PDF file includes:
Texts S1 to S12
Figs. S1 to S21
Table S1
References

REFERENCES AND NOTES

1. J. Ni, L. Li, Cathode architectures for rechargeable ion batteries: Progress and perspectives. *Adv. Mater.* **32**, 2000288 (2020).

2. J. Jiang, Y. Li, J. Liu, X. Huang, C. Yuan, X. W. Lou, Recent advances in metal oxide-based electrode architecture design for electrochemical energy storage. *Adv. Mater.* **24**, 5166–5180 (2012).

3. Y. Huang, Y. Fang, X. F. Lu, D. Luan, X. W. Lou, Co_3O_4 hollow nanoparticles embedded in mesoporous walls of carbon nanoboxes for efficient lithium storage. *Angew. Chem. Int. Ed.* **59**, 19914–19918 (2020).

4. P. Poizot, S. Laruelle, S. Grugeon, L. Dupont, J. M. Tarascon, Nano-sized transition-metal oxides as negative-electrode materials for lithium-ion batteries. *Nature* **407**, 496–499 (2000).

5. C. Yuan, H. B. Wu, Y. Xie, X. W. Lou, Mixed transition-metal oxides: Design, synthesis, and energy-related applications. *Angew. Chem. Int. Ed.* **53**, 1488–1504 (2014).

6. Z. Wang, L. Zhou, X. W. Lou, Metal oxide hollow nanostructures for lithium-ion batteries. *Adv. Mater.* **24**, 1903–1911 (2012).

7. S. Fang, D. Bresser, S. Passerini, Transition metal oxide anodes for electrochemical energy storage in lithium- and sodium-ion batteries. *Adv. Energy Mater.* **10**, 1902485 (2020).

8. H. You, S. Yang, B. Ding, H. Yang, Synthesis of colloidal metal and metal alloy nanoparticles for electrochemical energy applications. *Chem. Soc. Rev.* **42**, 2880–2904 (2013).

9. J. Lu, T. P. Wu, K. Amine, State-of-the-art characterization techniques for advanced lithium-ion batteries. *Nat. Energy* **2**, 17011–17024 (2017).

10. D. Chen, J. H. Wang, T. F. Chou, B. Zhao, M. A. El-Sayed, M. Liu, Unraveling the nature of anomalously fast energy storage in T-Nb_2O_5. *J. Am. Chem. Soc.* **139**, 7071–7081 (2017).

11. S. A. Farooqi, X. Wang, H. Lu, Q. Li, K. Tang, Y. Chen, C. Yan, Single-nanostructured electrochemical detection for intrinsic mechanism of energy storage: Progress and prospect. *Small* **14**, 1803482 (2018).

12. W. Si, I. Monch, C. Yan, J. Deng, S. Li, G. Lin, L. Han, Y. Mei, O. G. Schmidt, A single rolled-up Si tube battery for the study of electrochemical kinetics, electrical conductivity, and structural integrity. *Adv. Mater.* **26**, 7973–7978 (2014).

13. M. T. McDowell, Y. Cui, Single nanostructure electrochemical devices for studying electronic properties and structural changes in lithiated Si nanowires. *Adv. Energy Mater.* **1**, 894–900 (2011).

14. L. Mai, Y. Dong, L. Xu, C. Han, Single nanowire electrochemical devices. *Nano Lett.* **10**, 4273–4278 (2010).

15. A. Yang, G. Zhou, X. Kong, R. A. Vila, A. Pei, Y. Wu, X. Yu, X. Zheng, C. L. Wu, B. Liu, H. Chen, Y. Xu, D. Chen, Y. Li, S. Fakra, H. Y. Hwang, J. Qin, S. Chu, Y. Cui, Electrochemical generation of liquid and solid sulfur on two-dimensional layered materials with distinct areal capacities. *Nat. Nanotechnol.* **15**, 231–237 (2020).

16. C. P. Grey, J. M. Tarascon, Sustainability and in situ monitoring in battery development. *Nat. Mater.* **16**, 45–56 (2016).

17. G. Zhou, A. Yang, Y. Wang, G. Gao, A. Pei, X. Yu, Y. Zhu, L. Zong, B. Liu, J. Xu, N. Liu, J. Zhang, Y. Li, L. W. Wang, H. Y. Hwang, M. L. Brongersma, S. Chu, Y. Cui, Electrotunable liquid sulfur microdroplets. *Nat. Commun.* **11**, 606–615 (2020).

18. J. Wan, W. Bao, Y. Liu, J. Dai, F. Shen, L. Zhou, X. Cai, D. Urban, Y. Li, K. Jungjohann, M. S. Fuhrer, L. Hu, In situ investigations of Li-MoS₂ with planar batteries. *Adv. Energy Mater.* **5**, 1401742 (2015).

19. J. Y. Huang, L. Zhong, C. M. Wang, J. P. Sullivan, W. Xu, L. Q. Zhang, S. X. Mao, N. S. Hudak, X. H. Liu, A. Subramanian, H. Fan, L. Qi, A. Kushima, J. Li, In situ observation of the electrochemical lithiation of a single SnO₂ nanowire electrode. *Science* **330**, 1515–1520 (2010).

20. F. Gabler, D. D. Karnaushenko, D. Karnaushenko, O. G. Schmidt, Magnetic origami creates high performance micro devices. *Nat. Commun.* **10**, 3013–3023 (2019).

21. Y. Yin, S. Li, S. Böttner, F. Yuan, S. Giudicatti, E. Saei Ghareh Naz, L. Ma, O. G. Schmidt, Localized surface plasmons selectively coupled to resonant light in tubular microcavities. *Phys. Rev. Lett.* **116**, 253904 (2016).

22. Y. Yin, T. Qiu, L. B. Ma, X. Z. Lang, Y. Zhang, G. S. Huang, Y. F. Mei, O. G. Schmidt, Exploring rolled-up Au-Ag bimetallic microtubes for surface-enhanced Raman scattering sensor. *J. Phys. Chem. C* **116**, 25504–25508 (2012).

23. J. Zhang, J. Li, S. Tang, Y. Fang, J. Wang, G. Huang, R. Liu, L. Zheng, X. Cui, Y. Mei, Whispering-gallery nanocavity plasmon-enhanced Raman spectroscopy. *Sci. Rep.* **5**, 15012 (2015).

24. Z. Qu, M. Zhu, H. Tang, L. Liu, Y. Li, O. G. Schmidt, Towards high-performance microscale batteries: Configurations and optimization of electrode materials by in-situ analytical platforms. *Energy Storage Mater.* **29**, 17–41 (2020).

25. W. Huang, J. Zhou, P. J. Froeter, K. Walsh, S. Liu, M. D. Kraman, M. Li, J. A. Michaels, D. J. Sievers, S. Gong, X. Li, Three-dimensional radio-frequency transformers based on a self-rolled-up membrane platform. *Nat. Electron.* **1**, 305–313 (2018).

26. Y. F. Li, Y. H. Shi, S. G. Wang, J. H. Liu, J. Lin, Y. Xia, X. L. Wu, C. Y. Fan, J. P. Zhang, H. M. Xie, H. Z. Sun, Z. M. Su, Carbon/binder-free NiO@NiO/NF with in situ formed interlayer for high-areal-capacity lithium storage. *Adv. Energy Mater.* **9**, 1803690 (2019).

27. N. Mironova-Ulmane, A. Kuzmin, I. Steins, J. Grabis, I. Sildos, M. Pars, Raman scattering in nanosized nickel oxide NiO. *J. Phys. Conf. Ser.* **93**, 012039 (2007).

28. K. Fominykh, P. Chernev, I. Zaharieva, J. Sicklinger, G. Stefanic, M. Döblinger, A. Müller, A. Pokharel, S. Böcklein, C. Scheu, T. Bein, D. Fattakhova-Rohlfing, Iron-doped nickel oxide nanocrystals as highly efficient electrocatalysts for alkaline water splitting. *ACS Nano* **9**, 5180–5188 (2015).

29. Z. Yao, S. Kim, M. Aykol, Q. Li, J. Wu, J. He, C. Wolverton, Revealing the conversion mechanism of transition metal oxide electrodes during lithiation from first-principles. *Chem. Mater.* **29**, 9011–9022 (2017).

30. S. Thoufeeq, P. K. Rastogi, S. Thomas, A. Shravani, T. N. Narayanan, M. R. Anantharaman, Single step grown NiFe sponges as efficient water splitting electrocatalysts in alkaline medium. *ChemistrySelect* **5**, 1385–1395 (2020).

31. W. Wang, J. Qin, Z. Yin, M. Cao, Achieving fully reversible conversion in MoO₃ for lithium ion batteries by rational introduction of CoMoO₄. *ACS Nano* **10**, 10106–10116 (2016).

32. D. Bresser, F. Mueller, M. Fiedler, S. Krueger, R. Kloepsch, D. Baither, M. Winter, E. Paillard, S. Passerini, Transition-metal-doped zinc oxide nanoparticles as a new lithium-ion anode material. *Chem. Mater.* **25**, 4977–4985 (2013).

33. Y. Ma, C. Fang, B. Ding, G. Ji, J. Y. Lee, Fe-doped MnₓOᵧ with hierarchical porosity as a high-performance lithium-ion battery anode. *Adv. Mater.* **25**, 4646–4652 (2013).

34. W. Zhu, D. Liu, J. Trottier, C. Gagnon, J. Howe, A. Mauger, C. M. Julien, K. Zaghib, In-situ Raman spectroscopic investigation of LiMn₁.₄₅Ni₀.₄₅M₀.₁O₄ (M = Cr, Co) 5 V cathode materials. *J. Power Sources* **298**, 341–348 (2015).

35. D. Chen, X. Xiong, B. Zhao, M. A. Mahmoud, M. A. El-Sayed, M. Liu, Probing structural evolution and charge storage mechanism of NiO₂Hₓ electrode materials using in operando resonance Raman spectroscopy. *Adv. Sci.* **3**, 1500433 (2016).

36. X. Sun, C. Yan, Y. Chen, W. Si, J. Deng, S. Oswald, L. Liu, O. G. Schmidt, Three-dimensionally "curved" NiO nanomembranes as ultrahigh rate capability anodes for Li-ion batteries with long cycle lifetimes. *Adv. Energy Mater.* **4**, 1300912 (2014).

37. L. Cabo-Fernandez, F. Mueller, S. Passerini, L. J. Hardwick, In situ Raman spectroscopy of carbon-coated ZnFe₂O₄ anode material in Li-ion batteries—Investigation of SEI growth. *Chem. Commun.* **52**, 3970–3973 (2016).

38. Y. Zhou, M. Su, X. Yu, Y. Zhang, J. G. Wang, X. Ren, R. Cao, W. Xu, D. R. Baer, Y. Du, O. Borodin, Y. Wang, X. L. Wang, K. Xu, Z. Xu, C. Wang, Z. Zhu, Real-time mass spectrometric characterization of the solid-electrolyte interphase of a lithium-ion battery. *Nat. Nanotechnol.* **15**, 224–230 (2020).

39. A. Krause, O. Tkacheva, A. Omar, U. Langklotz, L. Giebeler, S. Dörfler, F. Fauth, T. Mikolajick, W. M. Weber, In situ Raman spectroscopy on silicon nanowire anodes integrated in lithium ion batteries. *J. Electrochem. Soc.* **166**, A5378–A5385 (2019).

40. C. Liu, H. Fu, Y. Pei, J. Wu, V. Pisharodi, Y. Hu, G. Gao, R. J. Yang, J. Yang, G. Cao, Understanding the electrochemical potential and diffusivity of MnO/C nanocomposites at various charge/discharge states. *J. Mater. Chem. A* **7**, 7831–7842 (2019).

41. E. Trevisanello, R. Ruess, G. Conforto, F. H. Richter, J. Janek, Polycrystalline and single crystalline NCM cathode materials-quantifying particle cracking, active surface area, and lithium diffusion. *Adv. Energy Mater.* **11**, 2003400 (2021).

42. R. C. O'Handley, *Modern Magnetic Materials: Principles and Applications* (Wiley, 2000).

43. W. Yan, W. Weng, G. Zhang, Z. Sun, Q. Liu, Z. Pan, Y. Guo, P. Xu, S. Wei, Y. Zhang, Structures and magnetic properties of (Fe, Li)-codoped NiO thin films. *Appl. Phys. Lett.* **92**, 052508 (2008).

44. C.-C. Chen, L. Fu, J. Maier, Synergistic, ultrafast mass storage and removal in artificial mixed conductors. *Nature* **536**, 159–164 (2016).

45. Y. Liu, T. Zhou, Y. Zheng, Z. He, C. Xiao, W. K. Pang, W. Tong, Y. Zou, B. Pan, Z. Guo, Y. Xie, Local electric field facilitates high-performance Li-ion batteries. *ACS Nano* **11**, 8519–8526 (2017).

46. Q. Li, H. Li, Q. Xia, Z. Hu, Y. Zhu, S. Yan, C. Ge, Q. Zhang, X. Wang, X. Shang, S. Fan, Y. Long, L. Gu, G. X. Miao, G. Yu, J. S. Moodera, Extra storage capacity in transition metal oxide lithium-ion batteries revealed by in situ magnetometry. *Nat. Mater.* **20**, 76–83 (2021).

47. X. Yin, H. Chen, C. Zhi, W. Sun, L. P. Lv, Y. Wang, Functionalized graphene quantum dot modification of yolk–shell NiO microspheres for superior lithium storage. *Small* **14**, 1800589 (2018).

48. J. Fu, W. Kang, X. Guo, H. Wen, T. Zeng, R. Yuan, C. Zhang, 3D hierarchically porous NiO/graphene hybrid paper anode for long-life and high rate cycling flexible Li-ion batteries. *J. Energy Chem.* **47**, 172–179 (2020).

49. C. Wang, Y. Zhao, D. Su, C. Ding, L. Wang, D. Yan, J. Li, H. Jin, Synthesis of NiO nano octahedron aggregates as high-performance anode materials for lithium ion batteries. *Electrochim. Acta* **231**, 272–278 (2017).

50. C. Heubner, M. Schneider, A. Michaelis, Diffusion-limited C-rate: A fundamental principle quantifying the intrinsic limits of Li-ion batteries. *Adv. Energy Mater.* **10**, 1902523 (2020).

51. P. Cendula, S. Kiravittaya, I. Monch, J. Schumann, O. G. Schmidt, Directional roll-up of nanomembranes mediated by wrinkling. *Nano Lett.* **11**, 236–240 (2011).

52. G. Kresse, J. Furthmüller, Efficient iterative schemes for ab initio total-energy calculations using a plane-wave basis set. *Phys. Rev. B* **54**, 11169–11186 (1996).

53. P. E. Blöchl, Projector augmented-wave method. *Phys. Rev. B* **50**, 17953–17979 (1994).

54. G. Kresse, D. Joubert, From ultrasoft pseudopotentials to the projector augmented-wave method. *Phys. Rev. B* **59**, 1758–1775 (1999).

55. J. P. Perdew, K. Burke, M. Ernzerhof, Generalized gradient approximation made simple. *Phys. Rev. Lett.* **77**, 3865–3868 (1996).

56. K. Momma, F. Izumi, *VESTA3* for three-dimensional visualization of crystal, volumetric and morphology data. *J. Appl. Cryst.* **44**, 1272–1276 (2011).

57. W. Zuo, C. Xie, P. Xu, Y. Li, J. Liu, A novel phase-transformation activation process toward Ni-Mn-O nanoprism arrays for 2.4 V ultrahigh-voltage aqueous supercapacitors. *Adv. Mater.* **29**, 1703463 (2017).

58. X. Sun, W. Si, X. Liu, J. Deng, L. Xi, L. Liu, C. Yan, O. G. Schmidt, Multifunctional Ni/NiO hybrid nanomembranes as anode materials for high-rate Li-ion batteries. *Nano Energy* **9**, 168–175 (2014).

59. Y. Wan, K. Song, W. Chen, C. Qin, X. Zhang, J. Zhang, H. Dai, Z. Hu, P. Yan, C. Liu, S. Sun, S. L. Chou, C. Shen, Ultra-high initial Coulombic efficiency induced by interface engineering enables rapid, stable sodium storage. *Angew. Chem. Int. Ed.* **60**, 11481–11486 (2021).

60. J. Liang, H. Hu, H. Park, C. Xiao, S. Ding, U. Paik, X. W. Lou, Construction of hybrid bowl-like structures by anchoring NiO nanosheets on flat carbon hollow particles with enhanced lithium storage properties. *Energ. Environ. Sci.* **8**, 1707–1711 (2015).

61. J. M. Jeong, B. G. Choi, S. C. Lee, K. G. Lee, S. J. Chang, Y. K. Han, Y. B. Lee, H. U. Lee, S. Kwon, G. Lee, C. S. Lee, Y. S. Huh, Hierarchical hollow spheres of Fe₂O₃ @polyaniline for lithium ion battery anodes. *Adv. Mater.* **25**, 6250–6255 (2013).

62. B. Varghese, M. V. Reddy, Z. Yanwu, C. S. Lit, T. C. Hoong, G. V. S. Rao, B. V. R. Chowdari, A. T. S. Wee, C. T. Lim, C. H. Sow, Fabrication of NiO nanowall electrodes for high performance lithium ion battery. *Chem. Mater.* **20**, 3360–3367 (2008).

63. Z. Qiu, Y. Ma, T. Edvinsson, In operando Raman investigation of Fe doping influence on catalytic NiO intermediates for enhanced overall water splitting. *Nano Energy* **66**, 104118 (2019).

64. K. H. Kim, T. Kim, Y. S. Choi, W. Lee, W. Choi, J. Yoon, J. S. Park, Y. Kwon, W.-S. Yoon, J. M. Kim, Revealing the unconventional lithium storage mechanism of ordered mesoporous NiO for lithium-ion batteries. *J. Power Sources* **526**, 231135 (2022).

65. F. Lin, D. Nordlund, T. C. Weng, Y. Zhu, C. Ban, R. M. Richards, H. L. Xin, Phase evolution for conversion reaction electrodes in lithium-ion batteries. *Nat. Commun.* **5**, 3358 (2014).

66. S. Laruelle, S. Grugeon, P. Poizot, M. Dolle, L. Dupont, J. M. Tarascon, On the origin of the extra electrochemical capacity displayed by MO/Li cells at low potential. *J. Electrochem. Soc.* **149**, A627 (2002).

67. J. Chen, Z. Wang, J. Mu, B. Ai, T. Zhang, W. Ge, L. Zhang, Enhanced lithium storage capability enabled by metal nickel dotted NiO-graphene composites. *J. Mater. Sci.* **54**, 1475–1487 (2019).

68. Y. Gao, T. Rojas, K. Wang, S. Liu, D. Wang, T. Chen, H. Wang, A. T. Ngo, D. Wang, Low-temperature and high-rate-charging lithium metal batteries enabled by an electrochemically active monolayer-regulated interface. *Nat. Energy* **5**, 534–542 (2020).